TIME-LAPSE FULL-WAVEFORM INVERSION FOR ELASTIC TTI MEDIA

YANHUA LIU[1],ILYA TSVANKIN[2]

[1]*Center for Wave Phenomena, Golden, CO 80401, USA*
[2]*Colorado School of Mines, Golden, CO 80401, USA*

(Received March 19, 2024; revised version accepted November 8, 2024)

ABSTRACT

Time-lapse (4D) full-waveform inversion (FWI) of seismic data can help estimate the subsurface changes due to hydrocarbon production and CO2 injection. Previously, we have developed a 4D FWI methodology for VTI (transversely isotropic with a vertical symmetry axis) media. However, the VTI algorithm fails to accurately reconstruct the 4D variations in the presence of dipping anisotropic layers that often cause a tilt of the symmetry axis. Here, we extend time-lapse FWI to 2D TI media with a tilted symmetry axis (TTI). The symmetry axis is assumed to be orthogonal to the reflectors, so its orientation can be es- timated from migrated depth images. The proposed algorithm is tested on the BP TTI model using three different time-lapse strategies. If the 4D data are repeatable, the param- eter changes can be reconstructed with sufficient accuracy even in the presence of moderate noise. We incorporate the "source-independent" FWI technique to mitigate the influence of errors in the estimated source wavelet and address the wavelet nonrepeatability in time- lapse data. In addition, we discuss the influence of several common nonrepeatability issues on the time-lapse inversion results. Testing on the BP model shows that the parallel- difference time-lapse method is more sensitive to nonrepeatability-related problems than the other employed 4D strategies.

KEY WORDS: Waveform inversion, Seismic anisotropy, Inverse theory

0963-0651/23/$5.00

INTRODUCTION

Time-lapse (4D) full-waveform inversion (FWI) is an important tool for monitoring sub- surface changes caused by hydrocarbon production and CO_2 injection with high spatial resolution (e.g., Lumley, 2010; Smith and Tsvankin, 2013; Vigh et al., 2014; Maharramov et al., 2016; Pevzner et al., 2017; Singh et al., 2018; Zhang and Alkhalifah, 2020; Li et al., 2021b,a). Instead of estimating time shifts or amplitude variations, 4D FWI inverts for the changes in the medium properties such as the P- and S-wave velocities. In addition, FWI uses different wave types (not just P-wave), which improves subsurface illumination and helps constrain more medium parameters. Moreover, an FWI image (the derivative of velocity model) often provides an improved alternative to conventional migration without employing tedious processing steps (Hicks et al., 2016; Arts et al., 2004; Davy et al., 2021). Using FWI image in time-lapse seismic makes it possible to avoid a number of preprocessing steps and provide more rapid turnaround to support reservoir management decisions.

Time-lapse FWI can be implemented in several different ways. Plessix et al. (2010) develop the parallel-difference (PD) 4D FWI strategy that inverts the baseline and mon- itor data independently using the same initial model. Another workflow (Routh et al., 2012) uses the inversion of the baseline survey to build the initial model for inverting the monitor data (sequential-difference strategy; SD), which improves the convergence of the monitor inversion. To increase the sensitivity of FWI to the changes inside the reservoir, Watanabe et al. (2004) and Denli and Huang (2009) suggest to directly invert the differencebetween the monitor and baseline data for the time-lapse parameter variations (double-difference strategy; DD). Zhou and Lumley (2021a) average the parameter variations pro- duced by forward (baseline to monitor) and reverse (monitor to baseline) applications of the sequential-difference strategy to reduce the dependence of the estimated time-lapse changes on the accuracy of the inverted baseline model (central-difference strategy; CD). However, the CD approach doubles the computational time compared to the SD and DD methods, typically without a significant improvement in resolution.

Most existing 4D FWI applications are limited to isotropic (often acoustic) media, which limits their applicability. Liu and Tsvankin (2021) extend the methodology of 4D FWI to VTI (transversely isotropic with a vertical symmetry axis) media and implement it with three different time-lapse strategies mentioned above (PD, SD, and DD). However, transversely isotropic layers (such as shales) may be dipping, which leads to a tilt of the symmetry axis (e.g., Tsvankin, 2012). For example, uptilted shale layers near salt domes produce an effective tilted TI (TTI) model, often with a large inclination of the symmetry axis.

As shown by a number of synthetic and field-data studies, VTI algorithms become inadequate in the presence of an even moderate symmetry-axis tilt.

For example, Behera and Tsvankin (2009) demonstrate that application of VTI velocity-analysis and imaging methods to data from TTI media may lead to significant misfocusing of reflectors and errors in parameter estimation. Wang and Tsvankin (2013) develop 2D P-wave reflectiontomography for TTI media and test it on field data from Volve field in the North Sea. Their results show that taking the symmetry-axis tilt into account significantly improves migrated images. Singh et al. (2021) apply an elastic TTI FWI algorithm to the Volve data set and incorporate facies constraints to regularize the inversion. However, to our knowledge, time-lapse FWI for elastic TTI media has not been discussed in the literature.

One of the challenges in FWI is its high sensitivity to the accuracy of the estimated source wavelet (Song et al., 1995; Pratt, 1999; Warner et al., 2013; Luo et al., 2014; Yuan et al., 2014). This issue is particularly significant for time-lapse FWI because the wavelet can change between the baseline and monitor surveys. Liu and Tsvankin (2022) incorporate a source-independent (SI) technique (Choi and Alkhalifah, 2011; Zhang et al., 2016; Bai and Tsvankin, 2019) into 4D FWI for VTI media and demonstrate its effectiveness in mitigating the influence of errors in the source wavelet on the obtained time-lapse parameter variations. Here, we apply the SI algorithm to time-lapse FWI for TTI media.

Another common issue in time-lapse seismic is the nonrepeatability (NR) of the baseline and monitor surveys. Ideally, the difference between the monitor and baseline data is caused only by the subsurface changes. However, the data difference can be distorted by a number of other factors. Zhou and Lumley (2021b) discuss the influence of several NR issues on time-lapse parameter inversion and the performance of 4D methods. However, their analysis is limited to isotropic acoustic media with known density, an inadequate model for many case studies.

Here, we extend the previously developed time-lapse VTI FWI algorithm to TTI media, which makes it suitable for a wider range of subsurface models. We begin by discussing the FWI methodology for anisotropic media and its application to time-lapse seismic data. Then we introduce a TTI FWI algorithm and implement it using three 4D strategies discussed above (PD, SD, and DD). The proposed methodology is tested on synthetic data for the section of the BP TTI model that includes an anticline. Then the source- independent method is incorporated into the TTI extension of the FWI algorithm to reduce the impact of distortions in the source signature. In addition, we analyze the influence of several other common nonrepeatability issues on 4D FWI implemented with several time- lapse strategies.

METHODOLOGY OF SOURCE-INDEPENDENT TIME-LAPSE FWI FOR TTI MEDIA

FWI for anisotropic media

Full-waveform inversion is designed to minimize the difference between the observed and simulated data, typically using the L_2-norm objective function $S(\mathbf{m})$ (e.g., Tarantola,1984):

$$S(\mathbf{m}) = \frac{1}{2}\left\|\mathbf{d}^{\mathrm{sim}}(\mathbf{m}) - \mathbf{d}^{\mathrm{obs}}\right\|^2, \tag{1}$$

where $\mathbf{d}^{\mathrm{sim}}$ is the data simulated for the model $\mathbf{m}$ and $\mathbf{d}^{\mathrm{obs}}$ is the observed data. Here, we minimize this objective function for multicomponent data from 2D TTI media.

We describe P- and SV-waves in TTI media using a velocity parameterization that was shown to reduce the trade-offs between the TI parameters (Kamath and Tsvankin, 2016). Also, the velocities (and their gradients) share the same units, which facilitates the optimization process. This notation includes the P- and S-wave velocities in the symmetry- axis direction (V_{P0} and V_{S0}), the P-wave velocity in the isotropy plane, which is orthogonal to the symmetry axis ($V_{hor,P}$), and the P-wave normal-moveout velocity from a horizontal reflector in the corresponding VTI medium ($V_{nmo,P}$). These four parameters along with density and the symmetry-axis tilt θ fully describe the signatures of P- and SV-waves in the vertical plane that contains the symmetry axis.

Following Kamath and Tsvankin (2016) and Liu and Tsvankin (2021), the adjoint-state method is used to calculate the gradient of the objective function $S(\mathbf{m})$ with respect to the model parameters. We employ a nonlinear conjugate-gradient method to iteratively update the medium parameters using the derivatives of the objective function expressed

$$\frac{\partial S(\mathbf{m})}{\partial \mathbf{m}} = -\left[\frac{\partial \mathbf{d}^{\mathrm{sim}}}{\partial \mathbf{m}}\right]\mathbf{q}\,, \tag{2}$$

where $\mathbf{q}$ is the residual wavefield. To find the optimal step length for all medium pa- rameters, we implement a line-searching algorithm which improves the convergence of the objective function near its minimum compared with the more conventional constant step- length method (K¨ohn et al., 2012). The step length is scaled by the ratio of the maximum values of the gradient to the medium parameter so that the model updates are consistent with the model value.

Forward modeling is based on the finite-difference solution of the elastic wave equation for heterogeneous TTI media:

$$\rho\frac{\partial^2 u_i}{\partial t^2} - \frac{\partial}{\partial x_j}\left[c_{ijkl}\frac{\partial u_k}{\partial x_l}\right] = f_i\,, \tag{3}$$

where **u** is the particle displacement, ρ is the density, c_{ijkl} is the stiffness tensor, and **f** is the density of the body forces. The wave equations for TTI and VTI media are described in more detail in Appendix A.

Strategies of time-lapse FWI

Time-lapse (4D) FWI operates with the baseline and monitor data sets. Here, we fo- cus on three common 4D FWI strategies discussed in the introduction: the parallel- difference (PD; Plessix et al., 2010), sequential-difference (SD; Asnaashari et al., 2012), and double-difference (DD; Denli and Huang, 2009; Waldhauser and Ellsworth, 2020) meth- ods. To operate directly with the observed ($\mathbf{d}^{obs} - \mathbf{d}^{obs}$) and simulated ($\mathbf{d}^{sim} - \mathbf{d}^{sim}$) data difference, the DD method (Figure 1) generates the "composite" data $\mathbf{d}_{com}$:

$$\triangle \mathbf{d} = (\mathbf{d}_{\mathrm{m}}^{\mathrm{obs}} - \mathbf{d}_{\mathrm{b}}^{\mathrm{obs}}) - (\mathbf{d}_{\mathrm{m}}^{\mathrm{sim}} - \mathbf{d}_{\mathrm{b}}^{\mathrm{sim}}) = \mathbf{d}_{\mathrm{com}} - \mathbf{d}_{\mathrm{m}}^{\mathrm{sim}} , \tag{4}$$

$$\mathbf{d}_{\mathrm{com}} = \mathbf{d}_{\mathrm{m}}^{\mathrm{obs}} - \mathbf{d}_{\mathrm{b}}^{\mathrm{obs}} + \mathbf{d}_{\mathrm{b}}^{\mathrm{sim}} , \tag{5}$$

where the subscripts "b" and "m" refer to the baseline and monitor data, respectively. The DD method estimates the parameters of the monitor model by minimizing $\triangle \mathbf{d}$ from equation 4; the initial monitor model is obtained by inverting the baseline data.

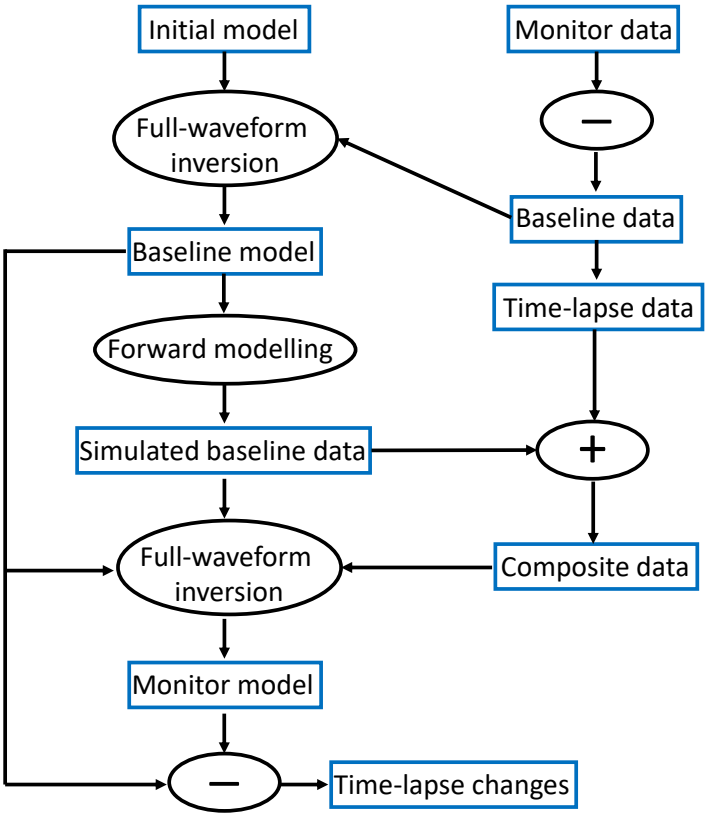

Figure 1: Workflow of the double-difference (DD) time-lapse strategy.

SYNTHETIC EXAMPLE

2D BP TTI model

The proposed time-lapse FWI algorithm is applied to the section of the 2D BP TTI model (Figure 2a-e), which contains an anticline. The model size is 4.5×1.8 km with a grid size of 10×10 m; the data are excited by 56 shots placed at a depth of 20 m with a constant interval of 80 m. There are 435 receivers on the sea floor at a depth of 210 m, which emulates ocean-bottom acquisition. The top of the model represents free surface, whereas for the other three boundaries we use the perfectly-matched-layers (PML) condi- tions. The maximum symmetry-axis tilt for this section of the BP model does not exceed 35° (Figure 3).

To obtain the initial model (Figures 2f-j), a Gaussian smoothing filter with a standard deviation of 70×70 m is applied to the actual parameter fields. Reflection tomography and/or borehole information can help build the initial model in field-data applications.

The monitor model is generated by reducing the baseline parameters V_{P0}, V_{S0}, and ρ in the target area (the thin horizontal layer) by 10% (Figures 2k, l, and m).

The input data are the vertical and horizontal particle velocities simulated using the elastic wave equation 3 for TTI media. FWI updates all parameters (the velocities and density) simultaneously. A multiscale approach with four frequency bands (2-5 Hz, 2-9 Hz, 2-13 Hz, and 2-19 Hz) is implemented to mitigate the cycle-skipping problem in FWI. The data below 2 Hz are excluded from the inversion because such low frequencies are usually unavailable in the field.

To estimate the tilt of the symmetry axis, we conduct depth migration for the initial baseline model and set the axis orthogonal to the reflectors (Wang and Tsvankin, 2013; Singh et al., 2021). Because the tilt for the BP model is mild, we employ VTI migration to generate a depth image using the updated medium parameters and apply a code (*sfdip*) from *Madagascar* (Fomel et al., 2013) to estimate the dips. This approach yields the results that are close to those obtained using TTI migration. An alternative way to generate a depth image for dip picking is to apply vertical differentiation to the velocity model obtained from high-frequency FWI (Davy et al., 2021), which also works well for our model. Because the symmetry-axis tilt is mild and does not change significantly over iterations, we update the tilt only after each inversion stage (frequency band) using the obtained structure dips.

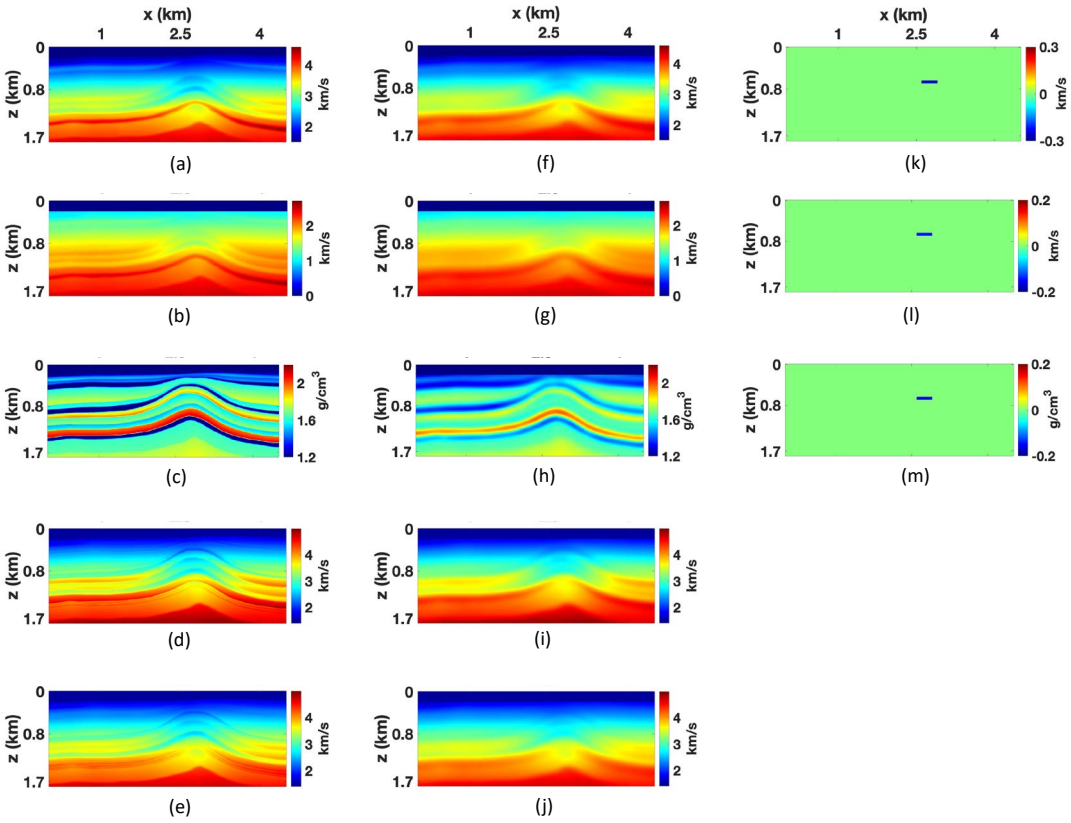

Figure 2: Parameters of the baseline BP TTI model with a grid size of 10 × 10 m: (a) the P-wave symmetry-axis velocity (V_{P0}), (b) the S-wave symmetry-axis velocity (V_{S0}), (c) the density (ρ), (d) the P-wave velocity in the isotropy plane ($V_{hor,P}$), and (e) the P-wave normal-moveout velocity ($V_{nmo,P}$). The initial baseline model of: (f) V_{P0}, (g) V_{S0}, (h) ρ, (i) $V_{hor,P}$, and (j) $V_{nmo,P}$. The actual time-lapse differences in (k) V_{P0}, (l) V_{S0}, and (m) ρ. Note that there are no time-lapse changes in $V_{hor,P}$ and $V_{nmo,P}$.

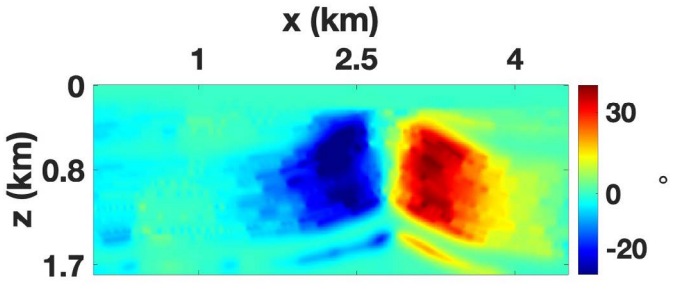

Figure 3: Tilt of the symmetry axis estimated by migrating the baseline data using the actual baseline model.

As mentioned above, we apply 4D FWI with the parallel-difference (PD), sequential- difference (SD), and double-difference (DD) strategies. The inverted baseline parameters are employed as the initial model in the monitor inversion in the SD and DD strategies without any smoothing. For the first test, the monitor data are acquired with perfect repeatability. The results (used below as the benchmark) show that all three strategies reconstruct 4D variations with sufficient spatial resolution (Figure 4). Because of the parameter trade-offs, the

time-lapse variations of $V_{\mathrm{hor,P}}$ and $V_{\mathrm{nmo,P}}$ (these velocities are unchanged) do not completely vanish. The DD strategy reconstructs the 4D variations with the highest resolution and generates the fewest errors outside the reservoir because the inversion of the monitor data operates with the actual 4D data difference. The SD and DD strategies are more computationally efficient and yield fewer artifacts than PD because the monitor inversion starts from the estimated baseline model.

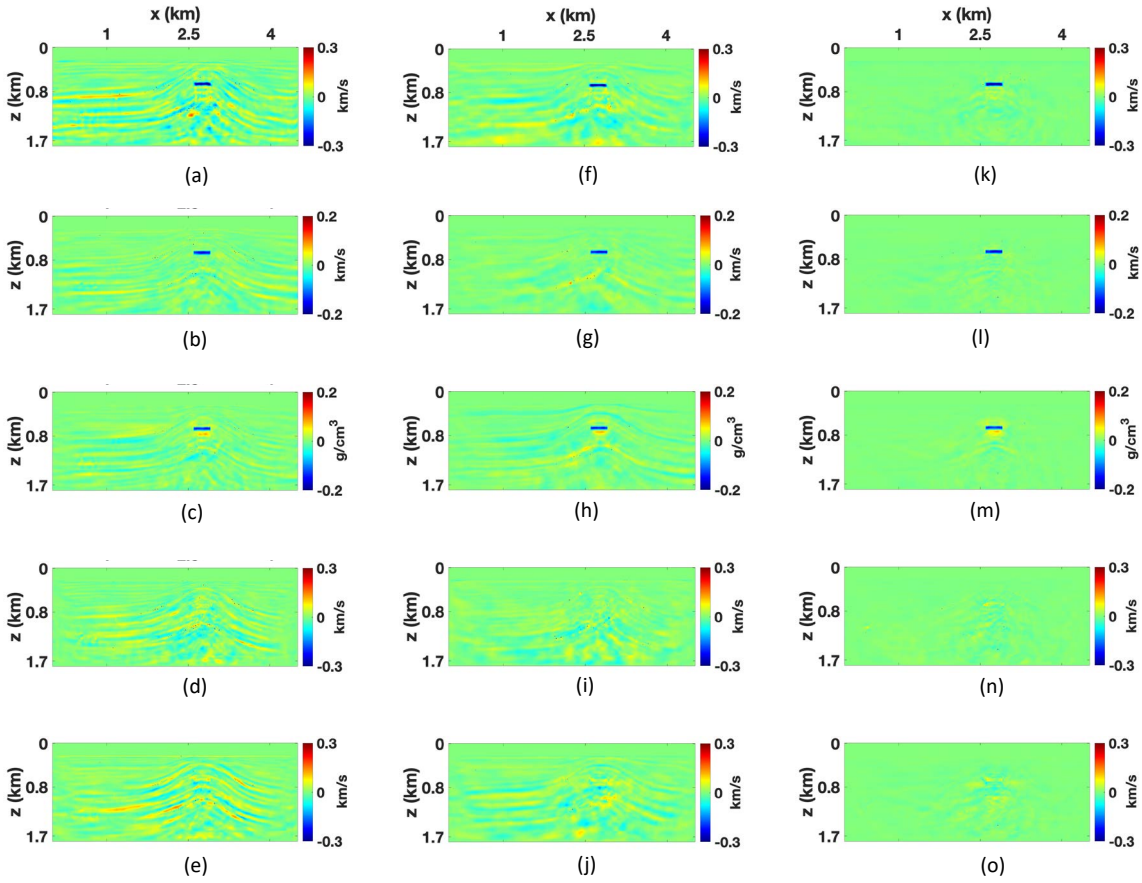

Figure 4: Time-lapse parameter variations obtained from the noise-free multicomponent data. The parallel-difference method: (a) V_{P0}, (b) V_{S0}, (c) ρ, (d) $V_{\mathrm{hor,P}}$, and (e) $V_{\mathrm{nmo,P}}$. The sequential-difference method: (f) V_{P0}, (g) V_{S0}, (h) ρ, (i) $V_{\mathrm{hor,P}}$, and (j) $V_{\mathrm{nmo,P}}$. The double-difference method: (k) V_{P0}, (l) V_{S0}, (m) ρ, (n) $V_{\mathrm{hor,P}}$, and (o) $V_{\mathrm{nmo,P}}$.

Influence of tilt

To evaluate the influence of the symmetry-axis tilt on the wavefield, we compare the ver- tical particle velocity simulated using the TTI and VTI algorithms for the actual baseline model (Figure 5). The reflected, diving, and converted waves computed for the two models match reasonably well for offsets smaller than 2 km because the tilt is relatively mild. The influence of tilt increases with the offset x and becomes more significant for waves that cross the dipping flanks of the anticline ($x \geq 2$ km) where the tilt is largest. Because the reservoir is subhorizontal (Figure 3), the VTI algorithm still resolves the parameter changes with acceptable accuracy.

Next, we design a different monitor model where the target layer is dipping and em- bedded in the left flank of the anticline (Figures 6a-c). After simulating the data for the actual TTI model, we conduct time-lapse FWI using the SD strategy. The 4D TTI al- gorithm accurately estimates the parameter changes in the reservoir (Figures 6i-m). In contrast, the size and magnitude of the time-lapse parameter variations (especially in ρ) are underestimated if the symmetry-axis tilt is ignored in FWI (Figures 6d-h). In addition, the VTI inversion generates significant false anomalies in all parameters along and below the anticline (red arrows). The inadequacy of the VTI model leads to parameter cross-talk that produces false anomalies in the velocities $V_{\text{hor,P}}$ and $V_{\text{nmo,P}}$ (which are held constant). Therefore, it is essential to apply the TTI FWI algorithm if the symmetry axis is tilted inside and around the reservoir, even if the tilt is relatively mild.

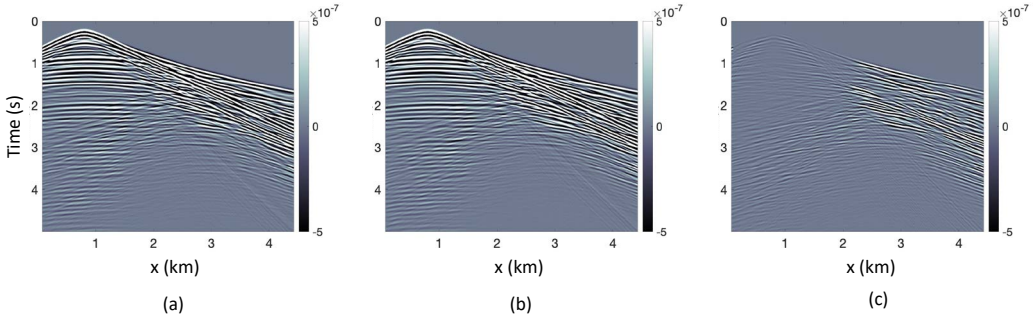

Figure 5: Shot gathers of the vertical particle velocity for: (a) the actual TTI medium, and (b) the corresponding VTI medium. Plot (c) shows the difference between plots (a) and (b).

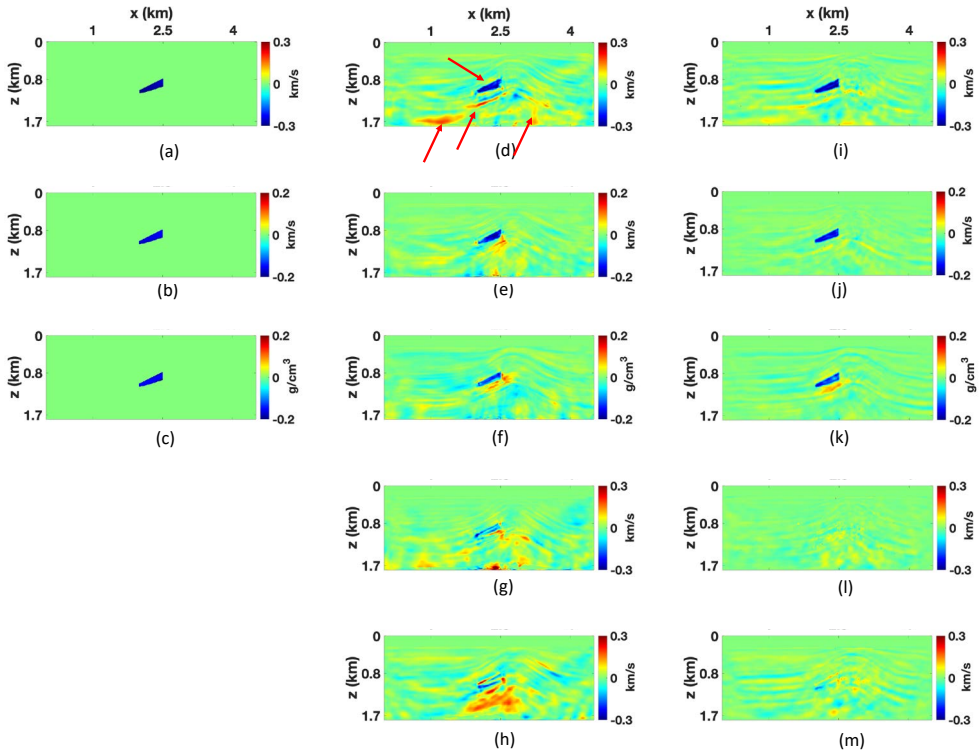

Figure 6: Time-lapse changes inside the reservoir located in a dipping segment of the anticline. The actual time-lapse changes: (a) V_{P0}, (b) V_{S0}, (c) ρ. The time-lapse variations estimated by the VTI [(d) V_{P0}, (e) V_{S0}, (f) ρ, (g) $V_{\text{hor,P}}$, and (h) $V_{\text{nmo,P}}$] and TTI [(i) V_{P0}, (j) V_{S0}, (k) ρ, (l) $V_{\text{hor,P}}$, and (m) $V_{\text{nmo,P}}$] algorithms. The red arrows point to the false anomalies produced by the VTI algorithm that does not take the symmetry-axis tilt into account.

Influence of nonrepeatable noise

To test the robustness of our method for noisy data, we add nonrepeatable random Gaus- sian noise with the signal-to-noise ratio (SNR) equal to 15 to both the baseline and monitor records for the model in Figure 2.

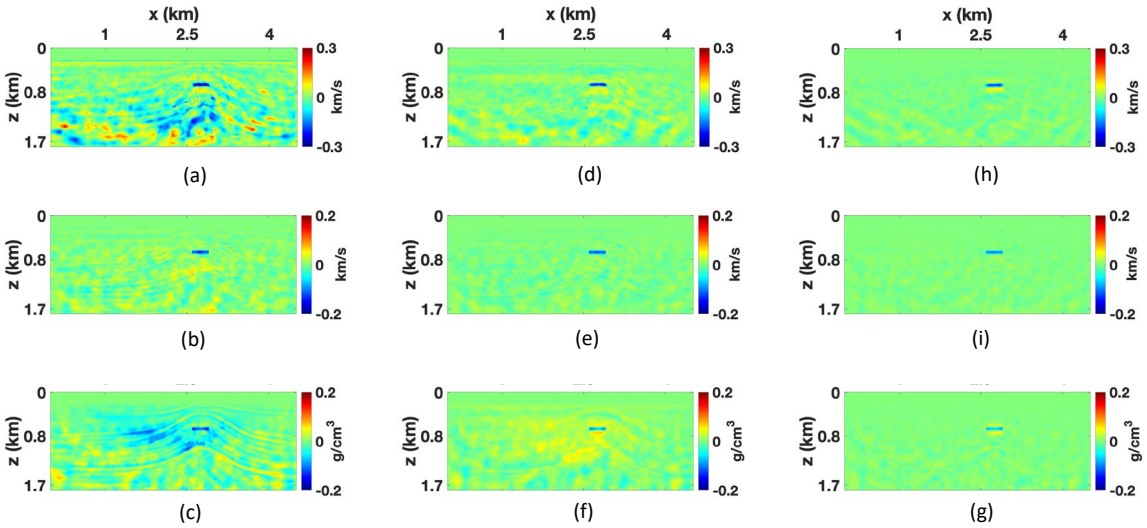

Figure 7: Time-lapse parameter variations obtained from noisy baseline and monitor data (the signal-to-noise ratio is 15) for the model in Figure 2. The parallel-difference strategy: (a) V_{P0}, (b) V_{S0}, and (c) ρ. The sequential-difference strategy: (d) V_{P0}, (e) V_{S0}, and (f) ρ. The double-difference strategy: (h) V_{P0}, (i) V_{S0}, and (j) ρ.

Figure 7 shows the inversion results for the parameters V_{P0}, V_{S0}, and ρ. As expected, the added noise degrades the reconstruction of the 4D variations (especially in ρ) and enhances parameter trade-offs. Similar to the noise-free test, the SD and DD strategies produce relatively few artifacts, whereas the noise-induced distortions are more pronounced in the output of the PD strategy. These observations are consistent with the results of Liu and Tsvankin (2021) for VTI media.

Influence of source wavelet

In 4D seismic processing, the source wavelet is usually estimated from the baseline data af- ter matching monitor and baseline records. However, wavelet extraction is time-consuming and error-prone, and the wavelets for the baseline and monitor data sets may differ. Errors in the wavelet distort the FWI results because they hinder matching of the observed and simulated data.

To analyze the influence of signal distortions, we carry out FWI using a wavelet (Wavelet1, Figure 8b) that substantially differs from the actual one (Figure 8a) in both phase and amplitude.

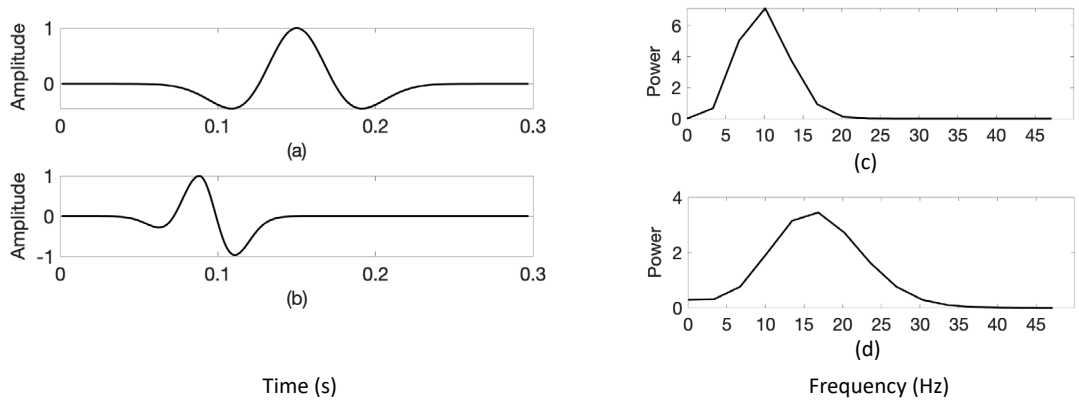

Figure 8: Source wavelets used in the synthetic examples: (a) the Ricker wavelet with a central frequency of 10 Hz (actual wavelet) and (b) the distorted "Ricker" wavelet with a central frequency of 17 Hz (Wavelet 1). The frequency spectra of: (c) the actual wavelet [see plot (a)] and (d) Wavelet 1 [see plot (b)].

First, we apply FWI to the baseline data using Wavelet 1. Because of the wavelet distortion, the model-updating algorithm could not converge to the global minimum of the objective function and reconstruct the anticline and the reservoir (Figures 9a-c). Such large errors make it clear that conventional FWI would not be able to estimate the time-lapse changes due to the wavelet distortions.

To reduce the dependence of the inversion results on the accuracy of the source sig- nal, we follow Liu and Tsvankin (2022) and implement the convolution-based source- independent (SI) objective function in the time domain (Choi and Alkhalifah, 2011). The SI algorithm (Figures 9d-f) dramatically improves the accuracy of the inverted parame- ters and reconstructs the baseline model with a resolution close to that of the benchmark sections (compare Figure 9d-f and Figures 9a-c).

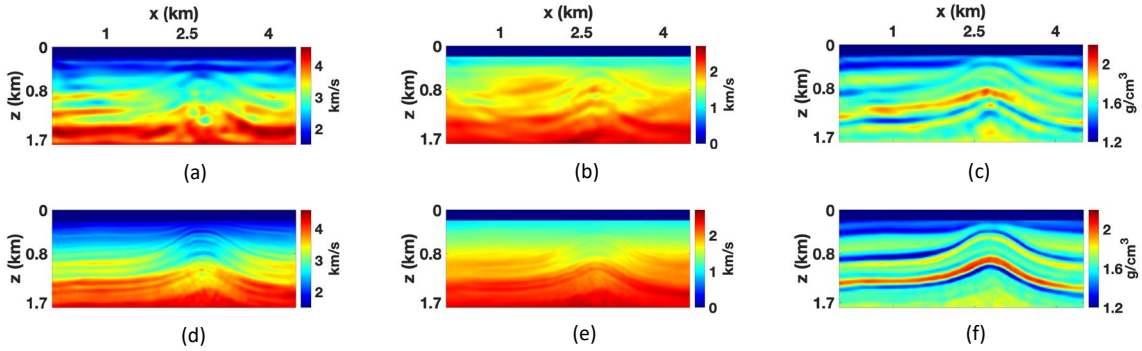

Figure 9: Baseline models estimated using Wavelet 1 by the conventional FWI [(a) V_{P0}, (b) V_{S0}, and (c) ρ] and the source-independent FWI algorithms [(d) V_{P0}, (e) V_{S0}, and (f) ρ].

Next we perform the monitor inversion using the source-independent algorithm with the PD and SD strategies and compute the time-lapse parameter variations. The DD method is not employed here because of the phase mismatch between the observed data and the data simulated for the inverted

baseline model using the distorted wavelet (Liu and Tsvankin, 2022). Despite underestimating the time-lapse changes inside the reservoir, the output of the PD and SD methods is sufficiently close to the benchmark sections, which is consistent with the results of Liu and Tsvankin (2022) for VTI media. Similar to the benchmark test, the SD workflow recovers the time-lapse changes with a higher resolution and fewer artifacts than the PD strategy (Figure 10). The SI methodology provides acceptable accuracy for noise-contaminated data with moderate levels of noise.

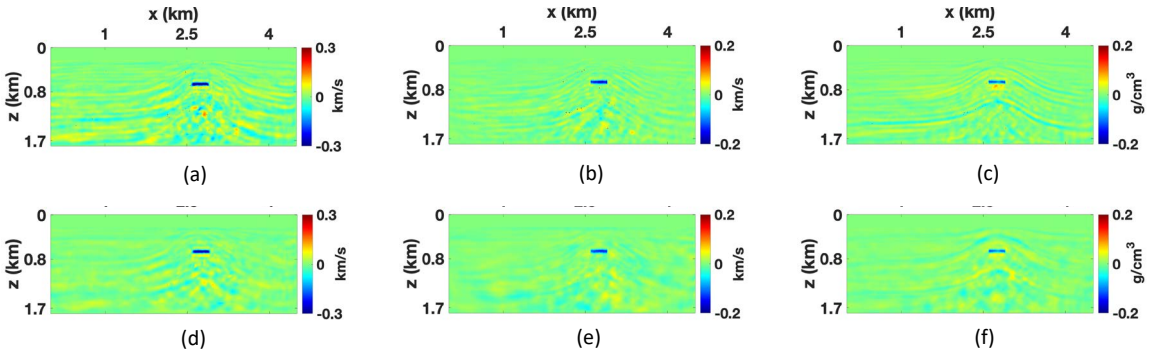

Figure 10: Time-lapse parameter variations reconstructed by the source-independent algorithm using Wavelet 1. The parallel-difference method: (a) V_{P0}, (b) V_{S0}, and (c) ρ. The sequential-difference method: (d) V_{P0}, (e) V_{S0}, and (f) ρ.

Influence of geometry nonrepeatability

The geometries of the baseline and monitor surveys are seldom perfectly repeatable, even for ocean-bottom-node (OBN) surveys where the nodes are equipped with ROV (Remotely Operated Vehicle) devices. Preprocessing can reduce the impact of the geometry NR but it is difficult to eliminate it completely. To explore the influence of the geometry changes on 4D FWI, we move each source in the monitor survey up and to the right by 10 m. Due to this source displacement, the data difference exhibits changes near and after the first arrival, which are unrelated to the actual time-lapse anomalies (Figure 11b).

First, 4D FWI is applied using the actual acquisition geometries. Not surprisingly, the shift in the source positions does not significantly influence the reconstruction of the time- lapse changes with all three time-lapse strategies (Figures 12a-c) because the baseline and monitor inversions are performed with the actual geometries. Although the DD strategy operates on the data difference, the error caused by the geometry changes cancels out in equation 4.

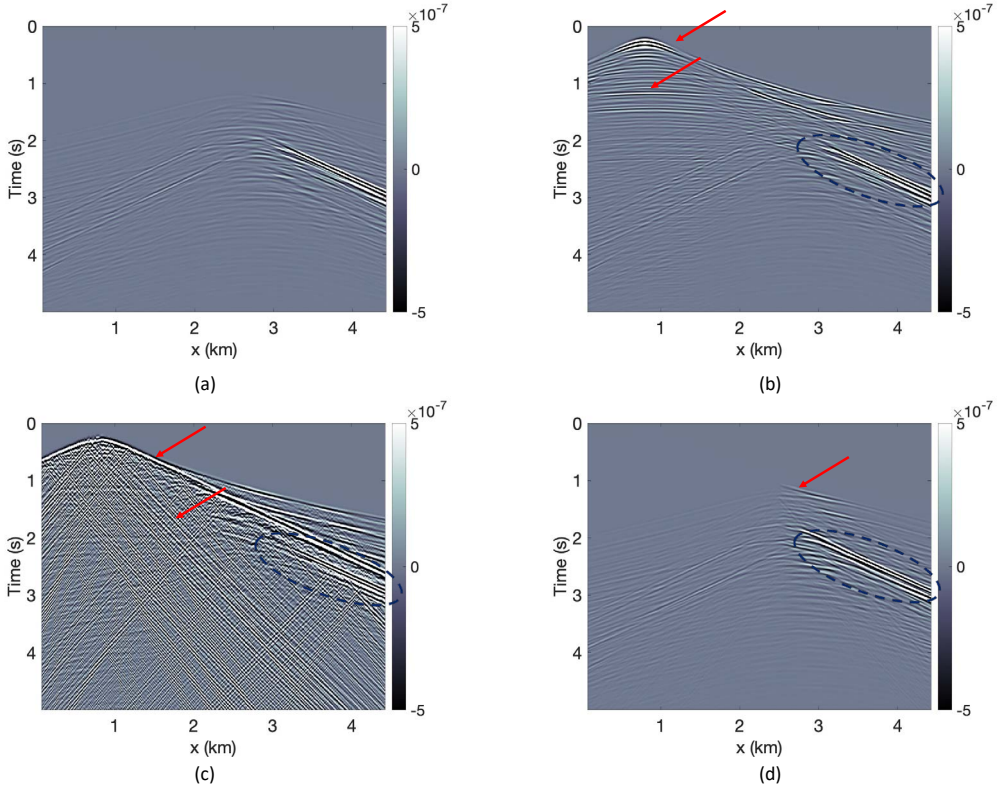

Figure 11: Difference between the vertical particle-velocity components from the monitor and baseline surveys for: (a) the perfectly repeatable data (referred to as the actual difference) and the data with (b) geometry nonrepeatability, (c) water velocity changes, and (d) overburden changes. The actual differences caused by the reservoir changes are circled in blue. The distortions caused by the nonrepeatability issues are marked by the red arrows.

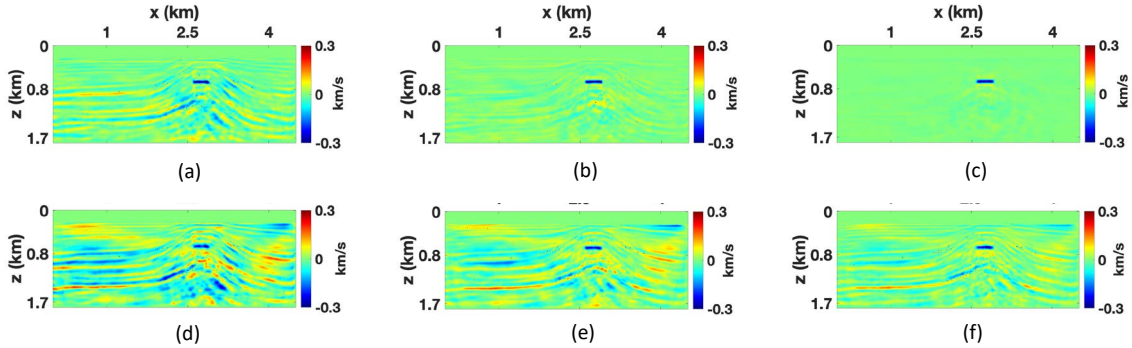

Figure 12: Time-lapse variations of the velocity V_{P0} estimated from the data with geometry nonrepeatability. The results obtained with the actual acquisition geometries: (a) the parallel-difference method, (b) the sequential-difference method, and (c) the double-difference method. The results obtained using the baseline geometry in the inversion of both the baseline and monitor data: (d) the parallel-difference method, (e) the sequential-difference method, and (f) the double-difference method.

Next, to evaluate the influence of geometry errors on the reconstructed 4D parameter variations, the baseline data are inverted using the actual geometry, whereas the monitor inversion is performed with the geometry of the baseline survey. Figures 12d-f show that all three time-lapse strategies produce significant artifacts in the 4D results because of the time shifts between the observed and

simulated monitor data caused by the geometry errors. In particularly, these time shifts lead to mispositioning of the reflectors due to the mismatch between these two data sets. Note that the PD strategy starts from a smoothed initial model (rather than the inverted baseline model) in the monitor inversion, which gives the model-updating algorithm more flexibility to misplace reflectors. Therefore, the parameter variations produced by the PD strategy (Figure 12d) are distorted more significantly by the geometry error compared to the two other strategies (Figures 12e and f), which agrees with the observation of Zhou and Lumley (2021b).

Influence of water statics

The water velocity may change between the baseline and monitor surveys, and the corre- sponding time shifts for some deep-water fields can reach 8 ms (Lecerf et al., 2022). Such "water statics" is often corrected by applying time shifts trace-by-trace before the inver- sion. However, those corrections may not be adequate for time-lapse FWI if the time-lapse parameter changes are relatively small (Borges et al., 2022). In the next test, we perturb the water velocity of the monitor model to generate time shifts up to 3 ms in the monitor data. Then both the baseline and monitor inversions are performed with the water velocity of the baseline model.

Figure 11c shows that the water velocity variations produce noticeable changes in the wavefields above the target area. Because of the incorrect water velocity for the monitor inversion, all three time-lapse strategies generate artifacts and underestimate the size of the reservoir and the amplitude of the parameter changes (Figure 13). Predictably, the parameters V_{P0} and ρ are distorted more than V_{S0} because there are no S-waves in the water. Similar to the geometry NR test above, the PD strategy yields the 4D results with the most artifacts. The SD and DD strategies produce comparable results, which indicates that these two approaches better handle moderate NR-related distortions.

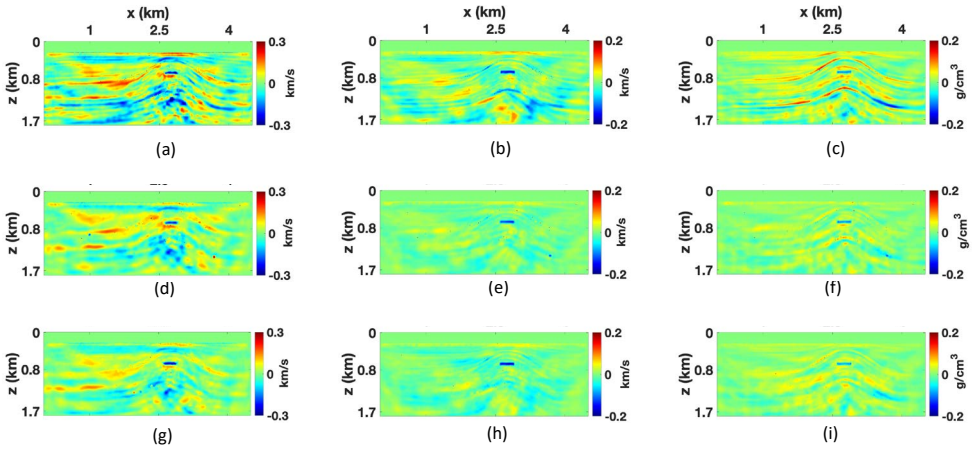

Figure 13: Time-lapse parameter variations estimated from the data with "water statics." The parallel-difference method: (a) V_{P0}, (b) V_{S0}, and (c) ρ. The sequential-difference method: (d) V_{P0}, (e) V_{S0}, and (f) ρ. The double-difference method: (g) V_{P0}, (h) V_{S0}, and (i) ρ.

Influence of overburden changes

Hydrocarbon production and CO_2 injection reduce the pore pressure inside the reservoir, which causes stress changes in the surrounding rocks (e.g., Smith and Tsvankin, 2012; Holt et al., 2016). These overburden and underburden changes produce time shifts that con- tain useful information for reservoir monitoring (e.g., Smith and Tsvankin, 2013). Precise modeling of stress-related velocity variations is beyond the scope of this paper, so here we simulate such overburden changes by simply increasing the baseline velocities V_{P0} and V_{S0} above the reservoir by up to 4% for the monitor survey (Figures 14a and b).

The influence of the overburden changes is visible in the difference between the monitor and baseline data (Figure 11d). Still, likely because the amplitude of the overburden veloc- ity changes is smaller than those in the reservoir, all three strategies are able to estimate the time-lapse variations in the reservoir and overburden with sufficient accuracy (Figure 14). Indeed, FWI is generally capable of reconstructing the entire model, although relatively large overburden anomalies could potentially mask those in the reservoir. Similar to the repeatability tests above, the DD strategy (Figures 14g and h) reconstructs the parameter changes with the highest resolution and fewest artifacts. This test also illustrates the sen- sitivity of our algorithm to relatively small changes in the overburden for input data with a relatively low noise level.

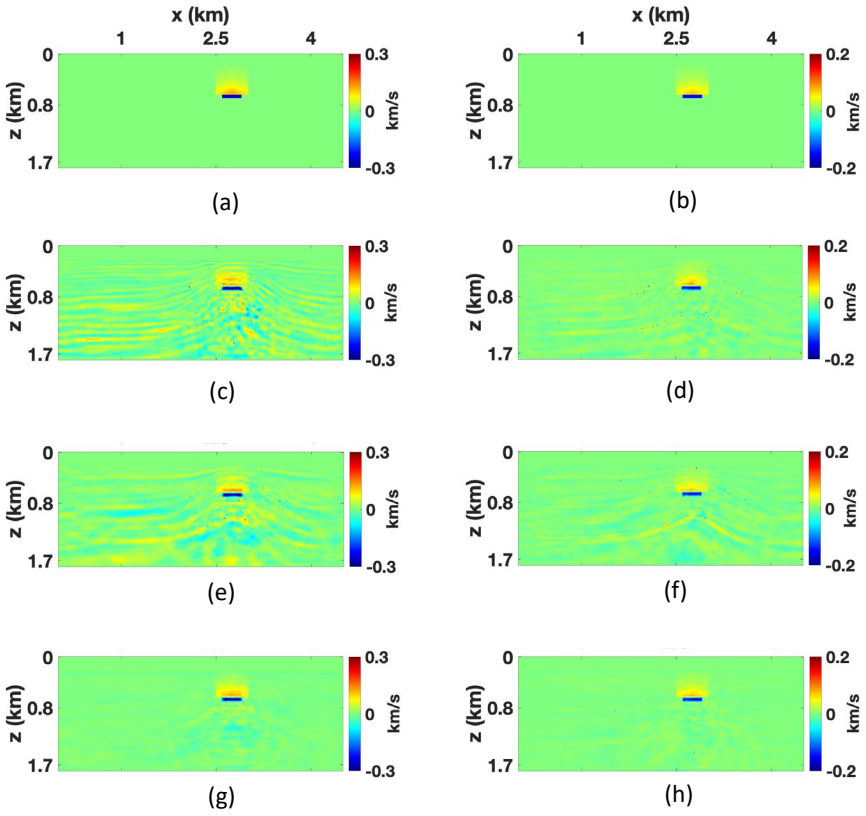

Figure 14: Time-lapse parameter variations for the data with overburden changes. The actual time-lapse variations in (a) V_{P0} and (b) V_{S0}. The parameter variations estimated by the parallel-difference strategy [(c) V_{P0} and (d) V_{S0}], the sequential-difference strategy [(e) V_{P0} and (f) V_{S0}], and the double-difference strategy [(g) V_{P0} and (h) V_{S0}].

DISCUSSION

We have demonstrated the ability of the proposed TTI algorithm to reconstruct velocities and density simultaneously, even in the presence of moderate noise. However, the forward modeling algorithm used in the inversion is the same as the one that generated the "ob- served" data. In reality, the ability of the proposed multiparameter inversion to reconstruct the medium parameters limited by the adequacy of the input seismic data and the assumed physical model.

FWI is a local optimization problem in the data domain designed to reduce the misfit between the field and simulated data. Therefore, the events in the field data which can not be reproduced by the modelling algorithm (e.g., noise) will contribute to the loss function and hamper model updates. A high signal-to-noise ratio and dense spatial sampling are necessary for FWI to overcome artifacts and reconstruct high-wavenumber velocity details. Additional problems can be caused by the inability of the forward-modeling algorithm and the initial model to reproduce the wave propagation the subsurface. For example, we have shown that application of a VTI FWI code to "observed" data generated for a TTI model produces significant artifacts.

In addition to the challenges in 3D FWI, the successful application of 4D FWI requires the time-lapse workflow to be able to handle the nonrepeatability between the baseline and monitor surveys. By comparing the performance of three different time-lapse strategies, we observed that the parallel-difference strategy (PD) requires a particularly high level of consistency between the baseline and monitor surveys. The step-sharing technique introduced by Fu and Innanen (2023) might be useful to mitigate this issue with the PD strategy. Alternatively, "joint" inversion (Alemie and Sacchi, 2016), which updates the baseline and monitor models simultaneously, may also improve the PD results.

The sequential- (SD) and double-difference (DD) strategies are more robust in the presence of NR issues. However, we observed that SD requires an accurate estimate of the baseline model. Otherwise, the monitor inversion focuses on updating the baseline residual rather than the actual data difference, which is consistent with the conclusion of Asnaashari et al. (2015). DD, on the other hand, is more robust than SD because the composite data contain the data simulated for the baseline model. Note that the performance of the time- lapse strategies varies with the type and quality of seismic data, the accuracy of the initial model, subsurface complexity, the size of the reservoir, and the amplitude of the time-lapse changes. Therefore, in field applications, it is advisable to test these workflows on a subset of the data prior to processing the entire survey.

CONCLUSIONS

We extended the previously developed time-lapse FWI methodology from VTI to TTI media, which makes it suitable for a wide range of subsurface

structures. The algorithm is tested on the anticlinal section of the BP TTI model using three different time-lapse strategies: the parallel- (PD), sequential- (SD), and double-difference (DD) workflows.

If the baseline and monitor data are sufficiently repeatable, our algorithm reconstructs the time-lapse variations of the TTI parameters with high spatial resolution, even in the presence of moderate noise.

We also incorporated the source-independent (SI) technique into FWI to mitigate the influence of errors in the estimated source wavelet on FWI and, in particular, on the time-lapse results. The SI FWI algorithm proved capable of reconstructing 4D parameter changes with sufficient accuracy even for a strongly distorted wavelet and noisy data. Employed with the PD and SD strategies, the SI FWI algorithm can alleviate the source- wavelet nonrepeatability (NR) issue in field-data applications.

In addition, we analyzed the impact on time-lapse FWI of other common NR problems, such as geometry changes, water statics, and time-lapse velocity variations in the overbur- den. In the test with different source locations for the baseline and monitor surveys, the time-lapse FWI algorithm that operated with the actual acquisition geometries accurately estimated the 4D changes. Water statics was shown not to have a significant influence on the inverted parameter variations, unless the corresponding time shifts are comparable to those caused by the reservoir changes. If stress-induced velocity changes in the overburden do not dominate the time-lapse response, FWI is capable of resolving the 4D parameter variations in the entire model including the reservoir.

ACKNOWLEDGMENTS

We thank the members of the Anisotropy-Team at the Center for Wave Phenomena (CWP) in the Geophysics Department at Colorado School of Mines for useful discussions. We also appreciate the comments from the editors and reviewers which help improve the manuscript. This work is supported by a joint project with INPEX Corporation and by the Consortium Project on Seismic Inverse Methods for Complex Structures at CWP.

DATA AND CODES AVAILABILITY

BP model can be downloaded from the SEG wiki Website

(*https* : *//wiki.seg.org/wiki/*2007 *BP Anisotropic V elocity Benchmark*).Codes associated with this research are available and can be obtained by contacting the corresponding au- thor.

AUTHOR CONTRIBUTIONS STATEMENT

I. Tsvankin proposed and supervised the research. Y. Liu conceived the design of the experiment(s). Y. Liu conducted the experiment(s). Y. Liu and I.

Tsvankin contributed ideas to the project, analyzed the results, and reviewed the manuscript.

REFERENCES

Alemie, W., and M. Sacchi, 2016, Joint reparametrized time-lapse full-waveform inversion: SEG Technical Program Expanded Abstracts, 1309–1314.

Arts, R., O. Eiken, A. Chadwick, P. Zweigel, L. van der Meer, and B. Zinszner, 2004, Monitoring of co2 injected at sleipner using time-lapse seismic data: Energy, **29**, 1383– 1392. (6th International Conference on Greenhouse Gas Control Technologies).

Asnaashari, A., R. Brossier, S. Garambois, F. Audebert, P. Thore, and J. Virieux, 2012, Time-lapse imaging using regularized FWI: a robustness study: SEG Technical Program Expanded Abstracts, 1–5., 2015, Time-lapse seismic imaging using regularized full-waveform inversion with a prior model: Which strategy?: Geophysical Prospecting, **63**, 78–98.

Bai, T., and I. Tsvankin, 2019, Source-independent waveform inversion for attenuation estimation in anisotropic media: Geophysical Prospecting, **67**, 2343–2357.

Behera, L., and I. Tsvankin, 2009, Migration velocity analysis for tilted transversely isotropic media: Geophysical Prospecting, **57**, 13–26.

Bond, W. L., 1943, The mathematics of the physical properties of crystals: The Bell System Technical Journal, **22**, 1–72.

Borges, F., M. Muzzette, L. E. Queiroz, B. Pereira-Dias, R. Dias, and A. Bulc˜ao, 2022, Analysis of water velocity changes in time-lapse ocean bottom acquisitions - A synthetic 2D study in Santos Basin, offshore Brazil: Journal of Applied Geophysics, **197**, 104521.

Choi, Y., and T. Alkhalifah, 2011, Source-independent time-domain waveform inversion using convolved wavefields: Application to the encoded multisource waveform inversion: Geophysics, **76**, no. 5, R125–R134.

Davy, R. G., L. Frahm, R. Bell, R. Arai, D. H. N. Barker, S. Henrys, N. Bangs, J. Mor- gan, and M. Warner, 2021, Generating high-fidelity reflection images directly from full- waveform inversion: Hikurangi subduction zone case study: Geophysical Research Let- ters, **48**, e2021GL094981.

Denli, H., and L. Huang, 2009, Double-difference elastic waveform tomography in the time domain: SEG Technical Program Expanded Abstracts, 2302–2306.

Fomel, S., P. Sava, I. Vlad, Y. Liu, and V. Bashkardin, 2013, Madagascar: Open-source software project for multidimensional data analysis and reproducible computational ex- periment: Journal of Open Research Software, **1**, e8.

Fu, X., and K. A. Innanen, 2023, Stepsize sharing in time-lapse full-waveform inversion: Geophysics, **88**, M59–M70.

Hicks, E., H. Hoeber, M. Houbiers, S. P. Lescoffit, A. Ratcliffe, and V. Vinje, 2016, Time- lapse full-waveform inversion as a reservoir-monitoring tool — A North Sea case study: The Leading Edge, **35**, 850–858.

Holt, R., A. Bauer, and A. Bakk, 2016, The importance of overburden stress path in assess- ment of stress dependence for 4D applications: European Association of Geoscientists & Engineers, 1–5.

Kamath, N., and I. Tsvankin, 2016, Elastic full-waveform inversion for VTI media: Method-ology and sensitivity analysis: Geophysics, **81**, no. 2, C53–C68.

K¨ohn, D., D. D. Nil, A. Kurzmann, A. Przebindowska, and T. Bohlen, 2012, On the influence of model parametrization in elastic full waveform tomography: Geophysical Journal International, **191**, 325–345.

Lecerf, D., M. Lange, A. Oates, and J. Kumar, 2022, Water column corrections: Joint water velocity inversion for 4d marine surveys: Second International Meeting for Applied Geoscience & Energy, 3404–3408.

Li, N., Z. Yu, R. To, M. Wang, Y. Xie, and D. Dickinson, 2021a, 4D FWI using towed- streamer data: A case study near Laverda oil field: SEG Technical Program Expanded Abstracts, 622–626.

Li, Y., T. Alkhalifah, and Q. Guo, 2021b, Target-oriented time-lapse waveform inversion using deep learning-assisted regularization: Geophysics, **86**, no. 4, R485–R495.

Liu, Y., and I. Tsvankin, 2021, Methodology of time-lapse elastic full-waveform inversion for VTI media: Journal of Seismic Exploration, **30**, 257–270. 2022, Source-independent time-lapse full-waveform inversion for anisotropic media: Geophysics, **87**, R111–R122.

Lumley, D., 2010, 4D seismic monitoring of CO_2 sequestration: The Leading Edge, **29**, no. 2, 150–155.

Luo, C. M., S. X. Wang, and S. Y. Yuan, 2014, Effect of inaccurate wavelet phase on prestack waveform inversion: Journal of Applied Geophysics, **11**, 479–488.

Maharramov, M., B. L. Biondi, and M. A. Meadows, 2016, Time-lapse inverse theory with applications: Geophysics, **81**, no. 6, R485–R501.

Pevzner, R., M. Urosevic, D. Popik, V. Shulakova, K. Tertyshnikov, E. Caspari, J. Correa,

T. Dance, A. Kepic, S. Glubokovskikh, S. Ziramov, B. Gurevich, R. Singh, M. Raab, M. Watson, T. Daley, M. Robertson, and B. Freifeld, 2017, 4D surface seismic tracks small supercritical CO2 injection into the subsurface: CO2CRC Otway Project: International Journal of Greenhouse Gas Control, **63**, 150–157.

Plessix, R.-E., S. Michelet, H. Rynja, H. Kuehl, C. Perkins, J. Maag, and P. Hatchell, 2010, Some 3D applications of full waveform inversion: EAGE Expanded Abstracts.

Pratt, R. G., 1999, Seismic waveform inversion in the frequency domain, part 1: Theory and verification in a physical scale model: Geophysics, **64**, 888–901.

Routh, P., G. Palacharla, I. Chikichev, and S. Lazaratos, 2012, Full wavefield inversion of time-lapse data for improved imaging and reservoir characterization: SEG Technical Program Expanded Abstracts, 1–6.

Singh, S., I. Tsvankin, and E. Z. Naeini, 2018, Bayesian framework for elastic full-waveform inversion with facies information: The Leading Edge, **37**,

924–931., 2021, Facies-based full-waveform inversion for anisotropic media: A North Sea case study: Geophysical Prospecting, **69**, 1650–1663.

Smith, S., and I. Tsvankin, 2012, Coupled geomechanical and seismic modeling of compaction-induced traveltime shifts for multi-component data: Geophysics, **77**, no. 6, 1687–1692.

Smith, S. S., and I. Tsvankin, 2013, Sensitivity of compaction-induced multicomponent seismic time shifts to variations in reservoir properties: Geophysics, **78**, no. 5, T151– T163.

Song, Z., P. R. Williamson, and R. G. Pratt, 1995, Frequency-domain acoustic-wave mod- eling and inversion of crosshole data: Part ii—inversion method, synthetic experiments and real-data results: Geophysics, **60**, 796–809.

Tarantola, A., 1984, Linearized inversion of seismic reflection data: Geophysical Prospect- ing, **32**, 998–1015.

Tsvankin, I., 2012, Seismic signatures and analysis of reflection data in anisotropic media, third edition: Society of Exploration Geophysicists.

Vigh, D., K. Jiao, D. Watts, and D. Sun, 2014, Elastic full-waveform inversion application using multicomponent measurements of seismic data collection: Geophysics, **79**, no. 2, R63–R77.

Waldhauser, F., and W. Ellsworth, 2020, A Double-difference Earthquake location algo- rithm: Method and application to the Northern Hayward Fault, California: Bulletin of the Seismological Society of America, **90**, no. 6, 1353–1368.

Wang, X., and I. Tsvankin, 2013, Multiparameter TTI tomography of P-wave reflection and VSP data: Geophysics, **78**, WC51–WC63.

Warner, M., A. Ratcliffe, T. Nangoo, J. Morgan, A. Umpleby, N. Shah, V. Vinje, I. Sˇtekl,

L. Guasch, C. Win, G. Conroy, and A. Bertrand, 2013, Anisotropic 3D full-waveform inversion: Geophysics, **78**, no. 2, R59–R80.

Watanabe, T., S. Shimizu, E. Asakawa, and T. Matsuoka, 2004, Differential waveform tomography for time-lapse crosswell seismic data with application to gas hydrate pro- duction monitoring: SEG Technical Program Expanded Abstracts, 2323–2326.

Yuan, F., S. Wang, S. Yuan, J. Wang, J. Li, P. Shi, and Y. Liu, 2014, Influence of inaccu- rate wavelet amplitude on frequency-domain full waveform inversion: EAGE Conference Expanded Abstracts, 1–5.

Zhang, Q., H. Zhou, Q. Li, H. Chen, and J. Wang, 2016, Robust source-independent elastic full-waveform inversion in the time domain: Geophysics, **81**, no. 2, R29–R44.

Zhang, Z., and T. Alkhalifah, 2020, High-resolution reservoir characterization using deep learning-aided elastic full-waveform inversion: The North Sea field data example: Geo- physics, **85**, no. 4, WA137–WA146.

Zhou, W., and D. Lumley, 2021a, Central-difference time-lapse 4D seismic full-waveform inversion: Geophysics, **86**, R161–R172. 2021b, Nonrepeatability effects on time-lapse 4D seismic full-waveform inversion for ocean-bottom node data: Geophysics, **86**, R547–R561.